Supplementary Information

Primary and Secondary Coordination Sphere Effects on the Structure and Function of *S*-nitrosylating Azurin

Casey Van Stappen,[1]* Huiguang Dai,[1,2] Anex Jose,[3] Shiliang Tian,[2] Edward I. Solomon,[3,4]* Yi Lu[1,2]*

[1]Department of Chemistry, University of Texas at Austin, 105 E 24th St., Austin, Texas 78712, United States

[2]Department of Chemistry and Biochemistry, University of Urbana-Champaign, Champaign, Illinois 61801, United States

[3]Department of Chemistry, Stanford University, Stanford, California 94305-5080, United States

[4]Stanford Synchrotron Radiation Lightsource, SLAC National Accelerator Laboratory, Menlo Park, California 94025, United States

*email: casey.vanstappen@utexas.edu, edward.solomon@stanford.edu yi.lu@utexas.edu

Table of Contents

Supplemental Methods ***2***

Site directed mutagenesis, Protein Expression **2**

EXAFS data processing **3**

QM/MM and *ab initio* calculations **3**

Supplemental Results ***5***

QM/MM Calculations **5**

Supplementary Figures ***10***

Supplementary Tables ***18***

Supplemental Methods

Site directed mutagenesis, Protein Expression

Plasmids containing the M121E (M121EAz), M121H/H46E (HEAz), M121H/H46E/N47S (HESAz), M121H/H46E/F114N (HENAz), M121H/H46E/F114N/N47S (HENSAz), and M121H/H46E/F114P (HEPAz) were constructed by site-directed mutagenesis using wild-type azurin (pET9a) as a template for the quick-change polymerase chain reaction procedure. Proteins were expressed in BL21(DE3) *E. coli* (Novagen, Madison, WI). Cultures were grown in LB media for 8 h at 37 °C and used to inoculate flasks containing 1.5 L of 2x YT media containing 50 mg/L Kanamycin (held in a 4 L flask) which were further grown at 25 °C while shaking at 210 rpm. These cultures were induced using IPTG (75mg/L final concentration) when an O.D of 0.5-0.6 was reached, approximately 15 hours. Cells were harvested 4.5 hours after induction and treated using an osmotic shock protocol. All steps of this protocol were performed at 4 °C, and all solutions were prepared using distilled, Milli-Q® EQ 7000 ultrapure filtered water: 1) Cells were resuspended in a solution of 20% sucrose solution (by mass) containing 30 mM Tris and 1 mM EDTA at pH 8 and placed on a shaker plate for 1.5 hours. 2) The sucrose cell suspension was centrifuged for 10 min. at 8000 rpm, and sucrose solution decanted off. The sucrose solution was placed in Spectra/Por® Dialysis Membrane tubing (MW cutoff: 3.5 kDa) and allowed to dialyze for 24-48 h in a 10 L solution of 30 mM NaOAc buffer (pH 4) containing 1 mM EDTA. 3) The cell pellet remaining from step 2 was resuspended in a freshly prepared solution of 1 mM dithiothreitol (DTT) solution containing 4 mM EDTA and vigorously shaken for 10 minutes, followed by centrifugation for 10 min. at 8000 rpm. The supernatant was decanted into an Erlenmeyer flask and stirred overnight while a solution of 320 mM NaOAc buffer (pH 4) (containing 1 mM EDTA) was added (equivalent to 10% of initial supernatant volume) via a peristaltic pump at a rate of 0.3 ml/min. 5) Solutions from both sucrose dialysis (step 2) and supernatant (step 4) were centrifuged further at 15000 rpm for 15 min. and passed through a 0.25 μM Amicon® before proceeding to purification steps. Proteins were purified by sequentially using 1) a SP Sepharose™ Fast Flow cation exchange column (40 ml bed volume) with a step-wise gradient using ammonium acetate buffer (50 mM) from pH 4 to pH 6, 2) a HiTrap™ QFF cation exchange column to remove any heme protein contamination (50 mM ammonium acetate), and finally 3) a size-exclusion column (500 ml bed volume, 25

mM Tris running buffer, pH 8). Samples buffer conditions and concentrations as described for specific samples were further prepared by using Cytiva PD10 Desalting Columns and EMD Amicon™ Ultra Centrifugal Filter Units with a 10 kDa molecular weight cutoff.

EXAFS data processing

Cu K-edge XAS spectra were splined from k = 0-15 Å^{-1} using an R-background of 1.0 and k-weight of 2. EXAFS fitting was performed using FEFF 8.0[1-3] via the software package Larch.[4] Possible scattering paths for EXAFS models were initially determined using FEFF 8.0 in combination with the reported crystal structure of M121H/H46E Az (PDB ID: 4WKX[5]) and QM/MM optimized structures obtained as described in the QM/MM methods section. Due to the already low-symmetry of the Cu binding site, fitting was limited to include only single scattering paths. Based on FEFF calculations, up to six significant single-scattering paths were identified, corresponding to short, mid, and long Cu-N/O, Cu-S, Cu-C (arising from C_δ of Glu), and Cu-C (arising from C_ε and C_γ of His). For all fits, the parameters R (bond distance), σ^2 (bond variance), and E_0 (ionization energy) were allowed to vary during fitting refinement. A fixed value of S_0^2 = 1.0 was used in all EXAFS fits. A k-range of 2-13 Å^{-1} and R-range of 1-3.2 Å was used in the curve fitting analysis of all spectra, providing a maximum resolution of ΔR = 0.143 Å and 15.4 degrees of freedom.

QM/MM and *ab initio* calculations

Quantum mechanics / molecular mechanics (QM/MM) models of each red copper azurin protein were performed based on the available crystal structure of M121H/H46E Az (PDB ID: 4KWX).[5] All QM/MM calculations were performed using ASH,[6] which provides an interface for the QM program ORCA,[7-8] version 5.0.3, with the MM program Open MM. MM calculations used the CHARMM36[9] forcefield. Protons were added for pH 7, and standard protonation states were assumed for all residues, including N_ε protonation of His117 and His121, deprotonation of Cys3 and Cys26 to form the cystine bond, and deprotonation of Cys112 to allow for Cu^{II} coordination. TIP3P water molecules were added to the protein using a 60 x 60 x 60 Å^3 solvation box, which included 7840 water molecules in total. Additionally, a total ionic strength of 0.1 was set using Na^+ as positive ions, and Cl^- as negative ions. Hydrogen positions were minimized using a 10000-step conjugate gradient algorithm,

and water positions relaxed using a 10000-step NVT simulation of 300 K using a periodic boundary condition.

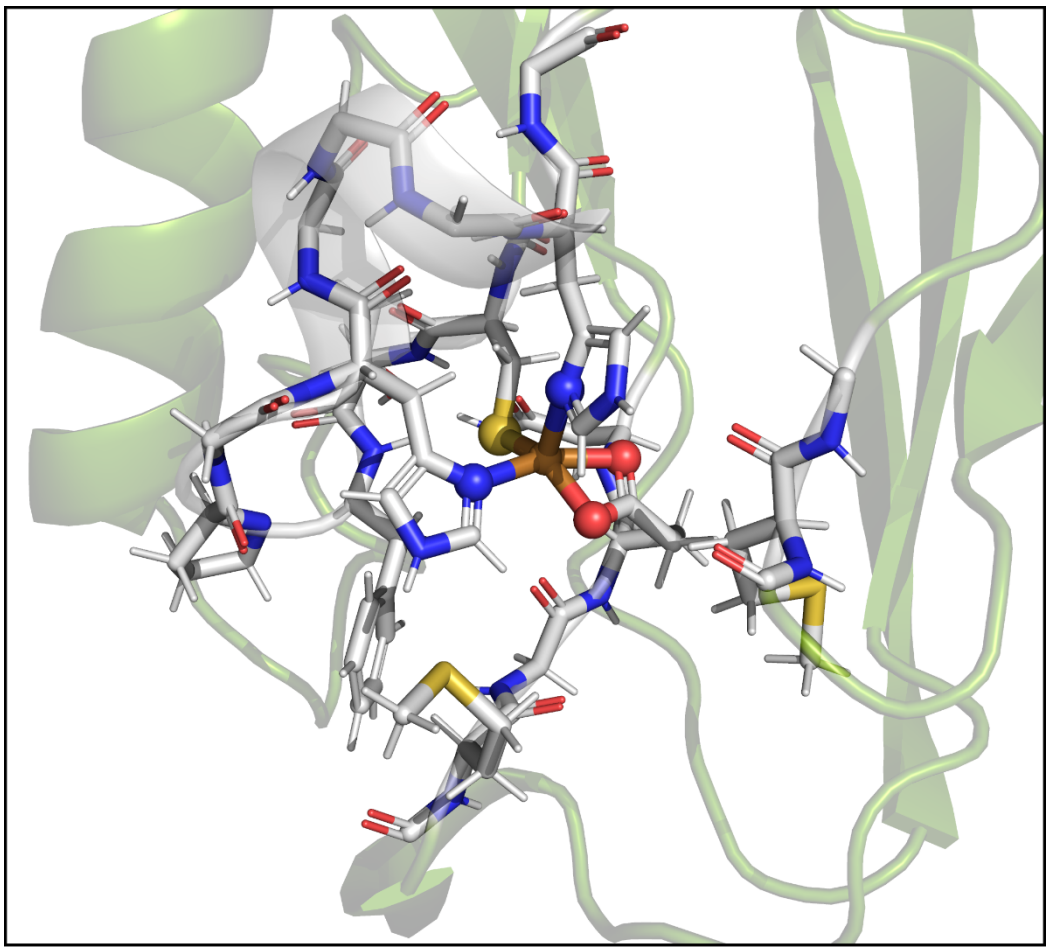

Figure SM-1. Diagram of large QM space employed in QM/MM calculations. Atoms included in the QM space are shown as sticks. Cu (orange), S (yellow), O (red) N (blue), C (light gray), H (white).

Two QM region selections were tested based on the extensive calibration series of Schulz, et al.[10] The smaller model includes Cu^{II}, Gly45-Asn47, Cys112-Phe114, and the sidechains of His117 and His121 (abbreviated to C_β), totaling 103 atoms (Figure SM-1). The large model includes Cu^{II}, Met13, the backbone of Gln14, Met44-Asn47, Cys112-His117, the amide backbone of Ser118-Leu120, His121, and the amide backbone of Lys122, totaling 215 atoms. Based on comparisons with the EXAFS analysis, reported calculated spectroscopic and electronic parameters in the main text and ESI have been made for calculations involving the larger QM space. For HEAz variants, substitutions of Asn47 and Phe114 for Ser47, Asn114, and Pro114 were made to generate the HESAz, HENAz, HENSAz, and HEPAz variants, for which there are no reported crystal structures. The QM/MM coupling was described using electrostatic embedding together with H link atoms and a charge-shifting scheme.[11]

All DFT-based QM calculations, including geometry optimization and partial Hessian calculations, used the TPSSh density functional,[12-13] with a D3BJ dispersion correction.[14-15] TPSSh was selected based on previous QM/MM computational studies of WTAz.[10] The DKH2 Hamiltonian was selected to account for relativistic effects.[16-19] Recontracted DKH-def2-TZVP(-f) basis sets were used for all atoms and all calculations,[20-21] along with decontracted def2/J basis sets for the RI approximation to the Coloumb intergals.[22] The chain of spheres approximation (COSX) was used for the exchange.[23] Vibrational frequencies were calculated using a numerical one-point formula partial Hessian approach (of varying size) for QM/MM.

DLPNO-CCSD(T) calculations were performed for the TPSSh-optimized large QM space on top of a TPSSh reference, with a corresponding point charge field generated from the MM space. Energy, spin density, and hyperfine coupling parameter calculations were performed using a previously established protocol involving the use of very tight thresholds for PNO generation together with decontraction of the basis sets,[24] which was further combined with a multifragment approach wherein different thresholds for PNO generation are used for “inner” and “outer” fragments.[10, 25] TightPNO thresholds were used for inner fragments including atoms for which HFCs were calculated as well as those bound to these atoms, whereas NormalPNO thresholds were used for all other atoms. Unrelaxed densities were used for DLPNO-CCSD derived spectroscopic properties.

Supplemental Results

QM/MM Calculations

To provide further insight into the electronic and geometric structure of the HEAz variants, a series of quantum mechanics/molecular mechanics (QM/MM) calculations were performed to generate optimized Cu active site geometries with an explicit description of the protein environment. The crystal structure of HEAz (PDB ID: 4WKX) was used as a starting point. A summary of calculated geometric parameters is provided in Table SR-1.

The average distances acquired via QM/MM are in good agreement with Cu K-edge EXAFS fits, but poor agreement with the reported crystal structure. As Cu^{II} is known to photoreduce in the presence of ionizing radiation, the QM/MM structure of Cu^{I}-HEAz was optimized for comparison. This Cu^{I}-QM/MM structure reproduces the reported crystal structure of HEAz well (Figure SR-1), reasonably matching both Cu

active site angles and distances. The most significant deviation is the relative contraction of the coordinating Cu-N_{117} bond, from 2.104 Å in the crystal structure to 1.955 Å to by QM/MM. Inspection of the 2fo-fc electron density map of 4WKX reveals an unusual elongation of the Cu-His117 distance, where the position of the imidazole sidechain can be better matched by a shorter Cu-N distance (Figure SR-1B). This mismatch arises from the global nature of crystallographic modeling, where an improved fit of the His117 sidechain is sacrificed in favor of better Ramachandran angles in the amide backbone.

Based on the good agreement EXAFS and our Cu^{II}-QM/MM for the Cu^{II} primary coordination sphere, we propose that the shorter, triply degenerate Cu-O/N(1) single scattering path used for the HESAz, HENAz, HENSAz, and HEPAz variants represents a composite of Cu-N_{H117}, Cu-N_{H121}, and the short Cu-O^{cis}_{E46} (positioned *cis* to the Cu-S); meanwhile, Cu-O/N(2) is correlated with Cu-O^{trans}_{E46} (positioned *trans* from the Cu-S) reflecting the denticity of Glu46. Averaging together these three calculated bond distances, the QM/MM models presented overestimate the Cu-O/N(1) scatterer by ~0.04 Å. Meanwhile, in HEAz, the complementing doubly-degenerate Cu-O/N(1) path for HEAz can be attributed to the equatorial Cu-N_{H117} and Cu-O^{cis}_{E46}, while the longer Cu-O/N(2) is a composite of both Cu-N_{H121} and Cu-O^{trans}_{E46} which lie outside the approximate equatorial plane. QM/MM calculated distances of HEAz averaging Cu-N_{H117} and Cu-O^{cis}_{E46} match the EXAFS Cu-O/N(1) within < 0.01 Å, while averaging Cu-N_{H121} and the second Cu-O^{trans}_{E46} overestimates Cu-O/N(2) by ~0.03 Å. We note that averaging the calculated Cu-N_{H117} and Cu-O^{cis}_{E46} distances reproduces the EXAFS-determined Cu-O/N(1) scatterer within ~0.01 Å in all cases; however, the experimental spectra lack the resolution to reasonably distinguish more than two scattering paths between Cu-N_{H117}, Cu-O^{cis}_{E46}, Cu-N_{H121}, and individually Cu-O^{cis}_{E46}.

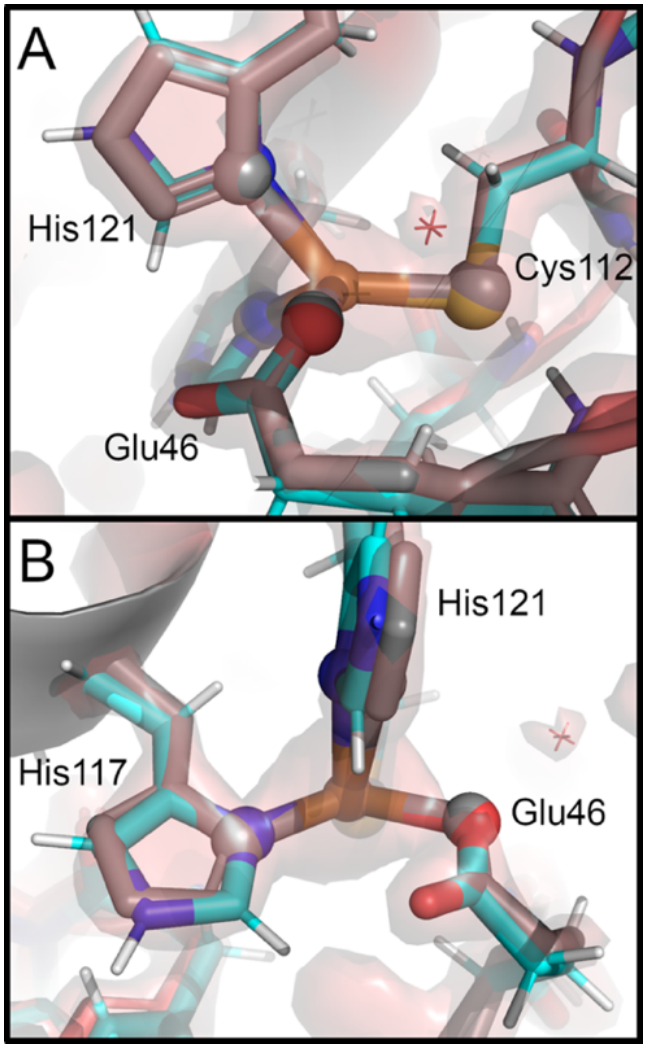

Figure SR-1. A) Side-on and B) rear-views of aligned 4WKX crystal (gray and salmon) and Cu^{I}-QM/MM optimized (cyan C, blue N, red O, yellow S) structures of HEAz. A semi-transparent overlay of the 2fo-fc electron density map of 4WKX is provided at 2σ.

The average QM/MM calculated Cu-S distances are estimated by ~0.02-0.04 Å for HEAz, HENAz, HENSAz, and HEPAz, while that of HESAz lies within < 0.01 Å of the EXAFS determined distance. Importantly, these calculations reasonably reproduce the significant contraction of Cu-S in HEP Az, caused by the removal of an H-bonding interaction between the 114 backbone amide and S via substitution of Phe for Pro.

Vibrational calculations using a numerical partial Hessian approach were employed to examine the Cu-S stretching bonds. The results are summarized in Table S4. All HEAz variants display a wide series of modes involving Cu and S displacement between ~260-350 cm^{-1}, with clearer Cu-S stretching modes ~290 and ~310 cm^{-1}. These computational results support the intensity-weighted average approach employed to analyze our resonance Raman results.

Table SR-1. Summary of select QM/MM calculated distances and angles for the HEAz variants. For WTAz,

Variant		$Cu\text{-}S_{112}$	$Cu\text{-}N_{117}$	$Cu\text{-}N_{121}$ ($Cu\text{-}N_{46}$ in WTAz)	$Cu\text{-}O_{46}(1)$	$Cu\text{-}O_{46}(2)$	$S_{112}\text{-}Cu\text{-}N_{117}$	$S_{112}\text{-}Cu\text{-}N_{121}$ ($S_{112}\text{-}Cu\text{-}N_{46}$ in WTAz)	$S_{112}\text{-}Cu\text{-}O_{46}(1)$	$S_{112}\text{-}Cu\text{-}O_{46}(2)$	$Cu\text{-}S_{112}\text{-}C_{\beta}$	$N_{121}\text{-}Cu\text{-}O_{46}(2)$
WTAz	XRD (4AZU)[a]	2.17	2.00	2.12	---	---	123.9	130.9	---	---	112.1	---
	EXAFS[b]	2.12	1.86/1.94	1.86/1.94	---	---						
HEAz	XRD	2.285	2.104	2.400	2.124	3.122	120.7	131.8	104.7	134.1	94.1	79.8
	EXAFS	2.27(1)	2.00	2.20	2.00	2.20						
	QM/MM(s)	2.252	1.911	2.667	2.087	2.129	107.5	113.5	93.8	143.8	100.4	
	Cu^{I}-QM/MM(I)	2.232	1.955	2.363	2.190	3.204	120.5	131.9	104.7	134.3	94.2	77.3
	QM/MM(I)	2.298	1.923	2.228	2.072	2.229	102.2	123.3	92.1	137.0	99.7	95.0
HESAz	EXAFS	2.30(1)		1.97		2.47						
	QM/MM(s)	2.304	1.936	2.407	2.028	2.124	102.1	117.8	93.2	143.3	99.0	
	QM/MM(I)	2.295	1.915	2.138	2.026	2.483	100.6	133.3	90.8	132.7	92.6	89.2
HENAz	EXAFS	2.26(1)		1.99		2.44						
	QM/MM(s)	2.315	1.943	2.083	2.056	2.400	96.5	145.2	92.02	121.3	93.2	
	QM/MM(I)	2.294	1.923	2.149	2.048	2.297	98.9	133.5	91.9	125.8	92.9	96.7
HENSAz	EXAFS	2.28(1)		1.98		2.55						
	QM/MM(s)	2.317	1.931	2.165	2.023	2.316	101.9	131.8	90.8	133.8	93.7	
	QM/MM(I)	2.320	1.940	2.052	2.075	2.367	100.4	138.0	87.6	121.8	94.5	93.3
HEPAz	EXAFS	2.24(1)		1.98		2.35						
	QM/MM(s)	2.254	1.989	2.171	2.079	2.202	97.3	120.8	90.8	141.4	110.0	
	QM/MM(I)	2.261	1.951	2.066	2.075	2.458	98.1	133.5	90.7	128.5	100.1	93.6

[a]Reference 26
[b]Reference 27

DFT-based methods are known to often overestimate metal-ligand covalency; therefore, DLPNO-CCSD(T) calculations were performed to determine accurate spin densities and hyperfine coupling constants. Technical details for these calculations are provided in the methods section of the ESI. These calculations both help us to better understand the distribution of spin across the Cu active site, as well as highlight discrepancies where theory fails to mirror experiment.

Table SR-2. Summary of spin population estimates as determined by extrapolation from different spectroscopic approaches**.** Calculated spin densities were determined by DLPNO-CCSD(T) calculations. Values for %Cu are derived directly from the parameter α^2 from CW-EPR; values of %S are derived directly from the S_p character of the SOMO determined by S K-edge measurements.

	SOMO Spin Densities					
	Cu		$S_{C112}(p)$		N_{H117}	O_{E46}
Variant	EPR	Calc.[a]	XAS	Calc.[a]	Calc.[a]	Calc.[a]
HEAz	73.6	73.1	18.6	12.6	7.1	6.4
HESAz	75.0	69.7	7.6	18.3	7.2	4.1
HENAz	68.7	69.7	18.6	17.0	7.3	5.5
HENSAz	71.2	72.4	12.2	12.7	7.9	4.7
HEPAz	77.7	70.7	15.2	18.1	6.6	3.9

[a]Mulliken spin densities
[b]Based on mirror treatment of DLPNO-CCSD(T) calculated hyperfine couplings

Generally, the DLPNO-CCSD(T) derived spin densities at Cu and S have a favorable comparison with our experimentally extrapolated estimates; for Cu, calculated spin densities appear within ~1% for HE, HEN, and HENS, while HES and HEP Az are underestimated by up to 7%. Similarly, the calculated spin densities of HEN, HENS and HEP Az are reasonably approximated relative to the S K-edge experiment (within 3% deviation). However, HE Az is significantly underestimated (6%) and HES Az overestimated (10%).

In summary, while our QM/MM calculations of the HE Az variants are unable to fully reproduce the relative trends observed with varying secondary coordination sphere mutations, our result *do* support our spectroscopic analyses, particularly for the Cu K-edge EXAFS, and resonance Raman spectroscopies.

Supplementary Figures

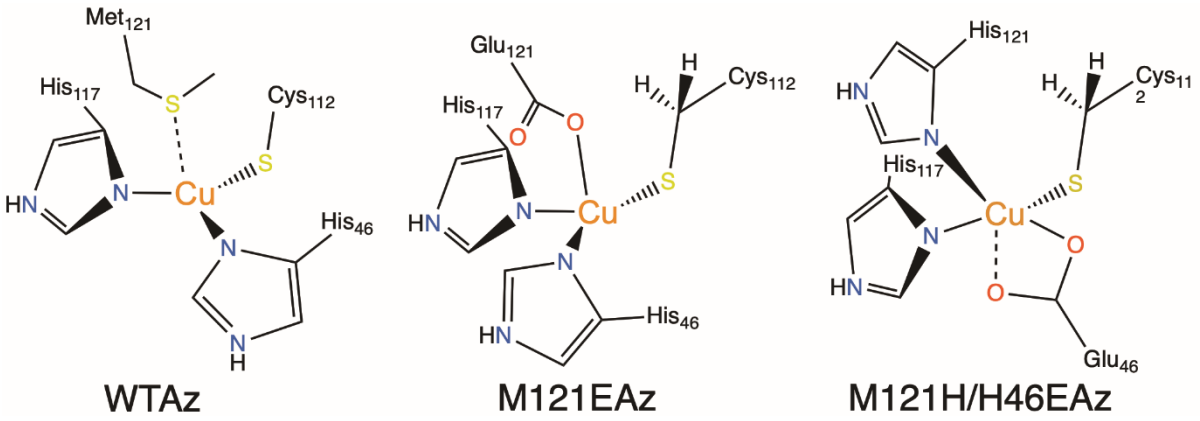

Figure S1. Comparison of proposed primary coordination sphere environments for WTAz, M121EAz, and M121H/H46EAz variants.

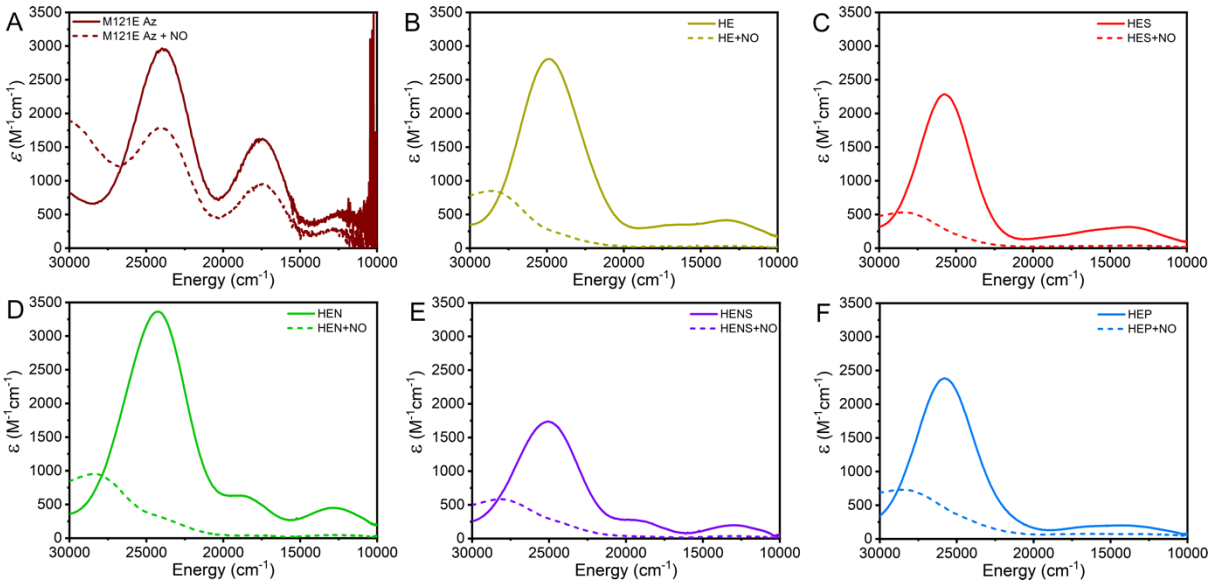

Figure S2. Comparisons of Az variants before and after reaction with NO. A) M121EAz, B) HEAz, C) HESAz, D) HENAz, E) HENSAz, F) HEPAz. Samples were prepared anoxically by reacting protein (100 μM) with 2 equiv. DEAE-NONOate (3 equiv. NO) for 500 s in 50 mM MES buffer, pH 6.0.

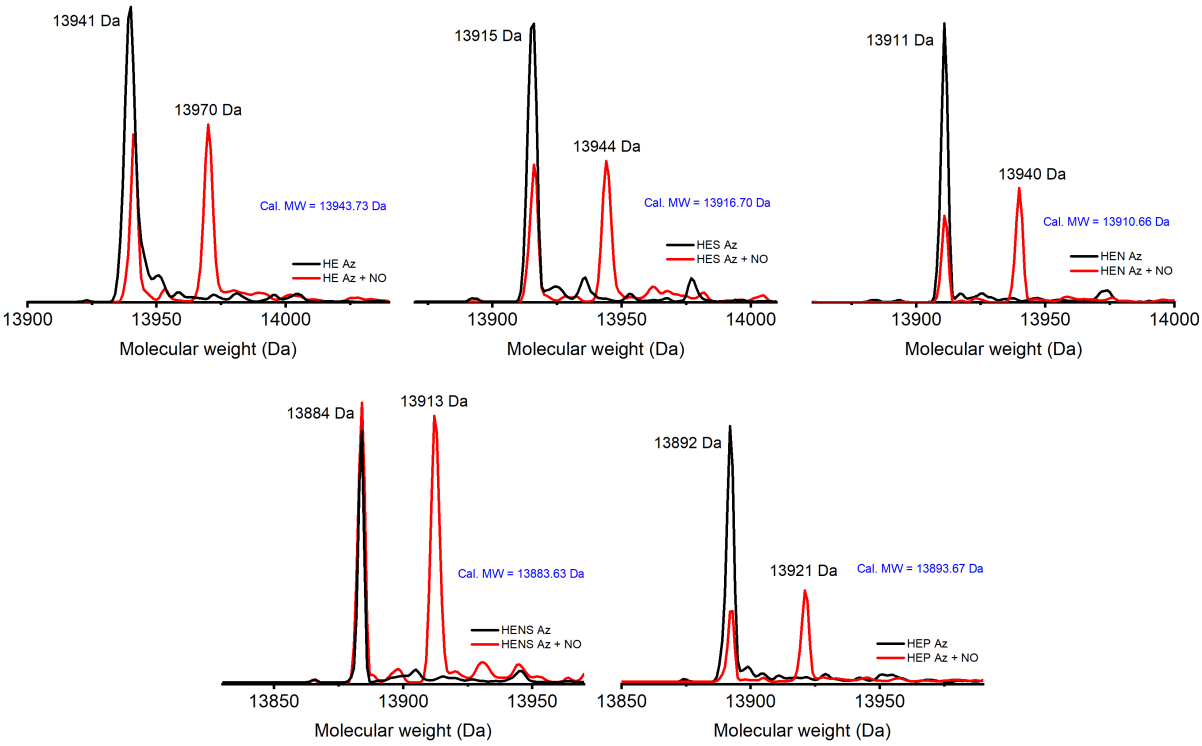

Figure S3. Mass spectrometry of HEAz variants before (black) and after (red) reaction with NO.

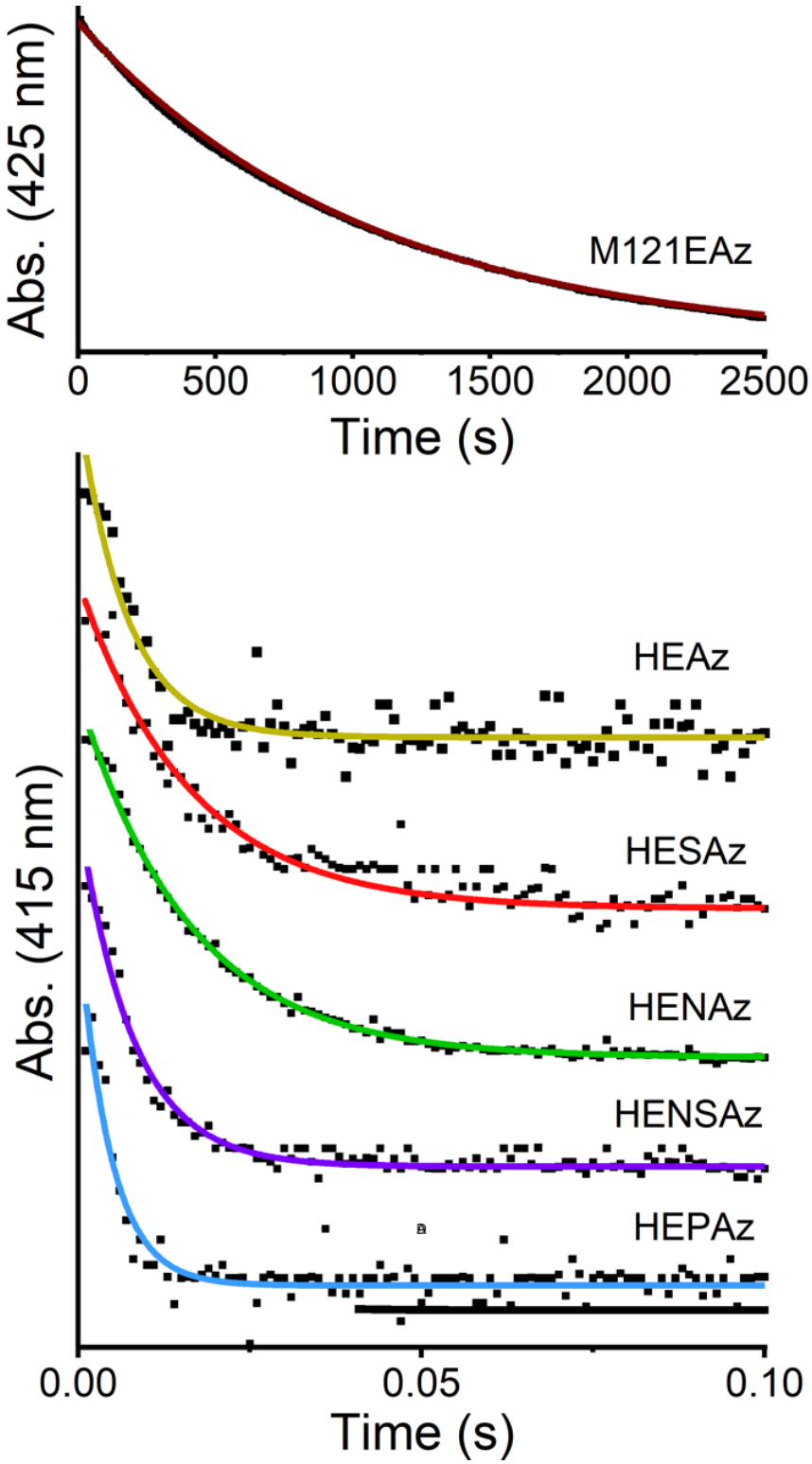

Figure S4. Transient absorption of (top) M121EAz (425 nm) (bottom) HEAz, HESAz, HENAz, HENSAz, and HEPAz (415 nm) under *pseudo* first-order conditions. Fits were performed using a *pseudo* first-order kinetic model, and are provided as colored, solid lines.

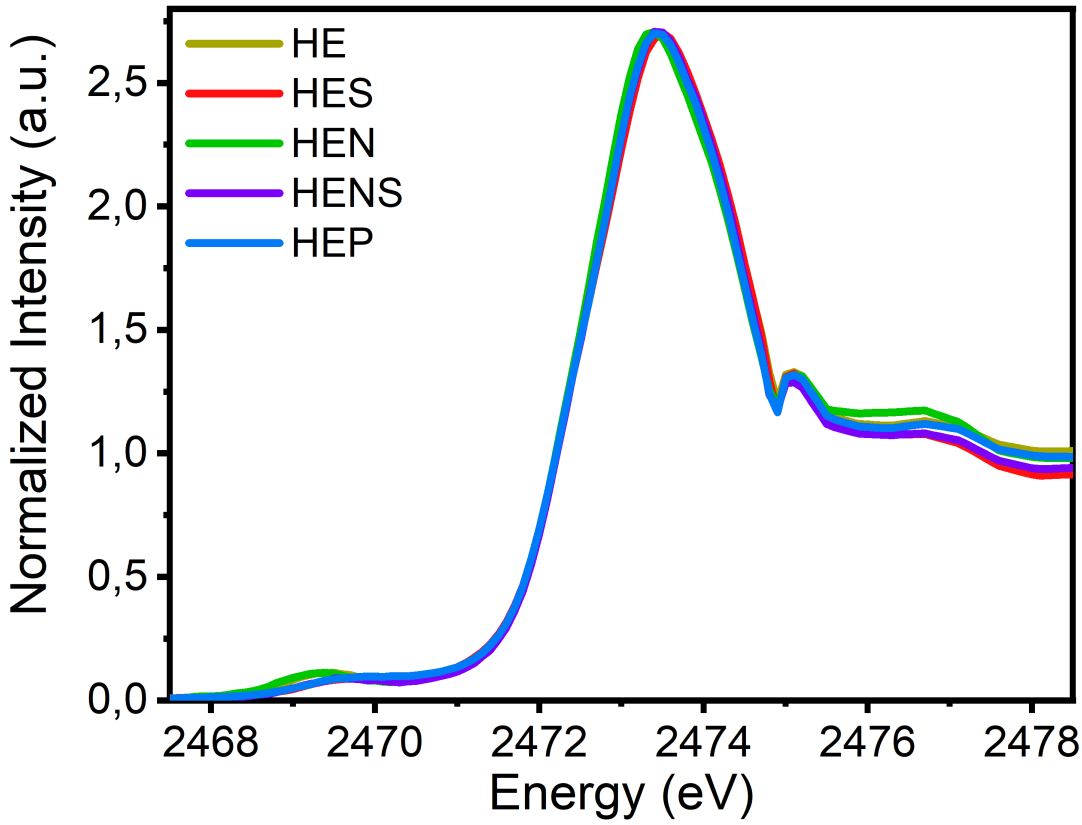

Figure S5. S K-edge XAS spectra of HEAz variants showing normalized edge.

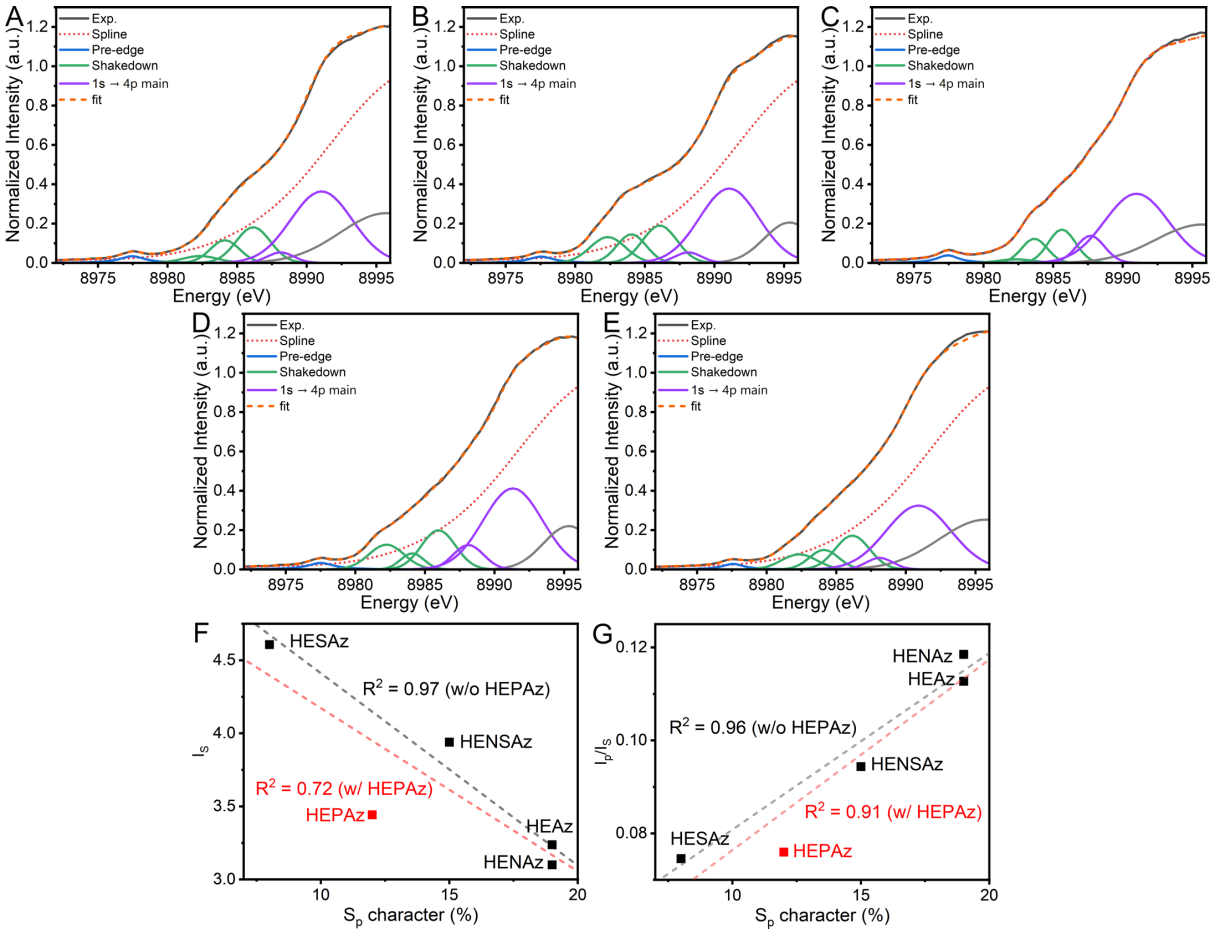

Figure S6. Cu K-edge XAS band deconvolution analysis of the HEAz variants A) HEAz, B) HESAz, C) HENAz, D) HENSAz, and E) HEPAz. All fitting was performed for normalized spectra; a summary of fit bands is provided in Table S2. Due to strong dependence of fit band intensities on the background spline and the similar edge shape between the five variants, an identical universal spline was applied to all spectra (dotted, red). Bands in the 8979-8987 eV are assigned as shakedown features based on previous studies of stellacyanin, WTAz, and plastocyanin.[28-29] Correlations between $\%S_p$ character (Table 2 of main text) are provided with F) the integrated intensity of the collectively assigned shakedown features (I_S), and G) the ratio of integrated pre-edge intensity (I_p) to the shakedown intensity, represented as I_p/I_S.

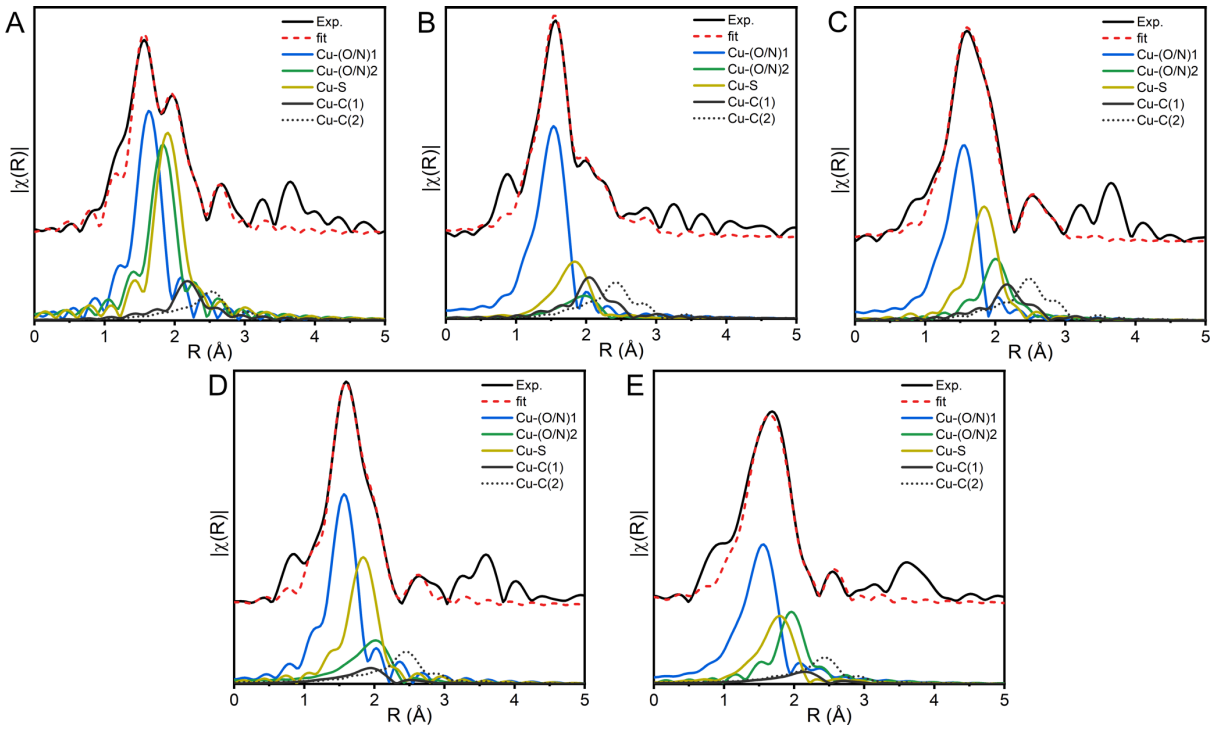

Figure S7. Comparison of Cu K-edge EXAFS spectra in R-space of HEAz variants A) HEAz, B) HESAz, C) HENAz, D) HENSAz, E) HEPAz. Fits corresponding to Table 5 (main text) are shown as dashed colored lines. Spectra are k^3-weighted, and FTs for all spectra were performed across a *k*-range of 2-13 Å^{-1}. No phase shift has been applied.

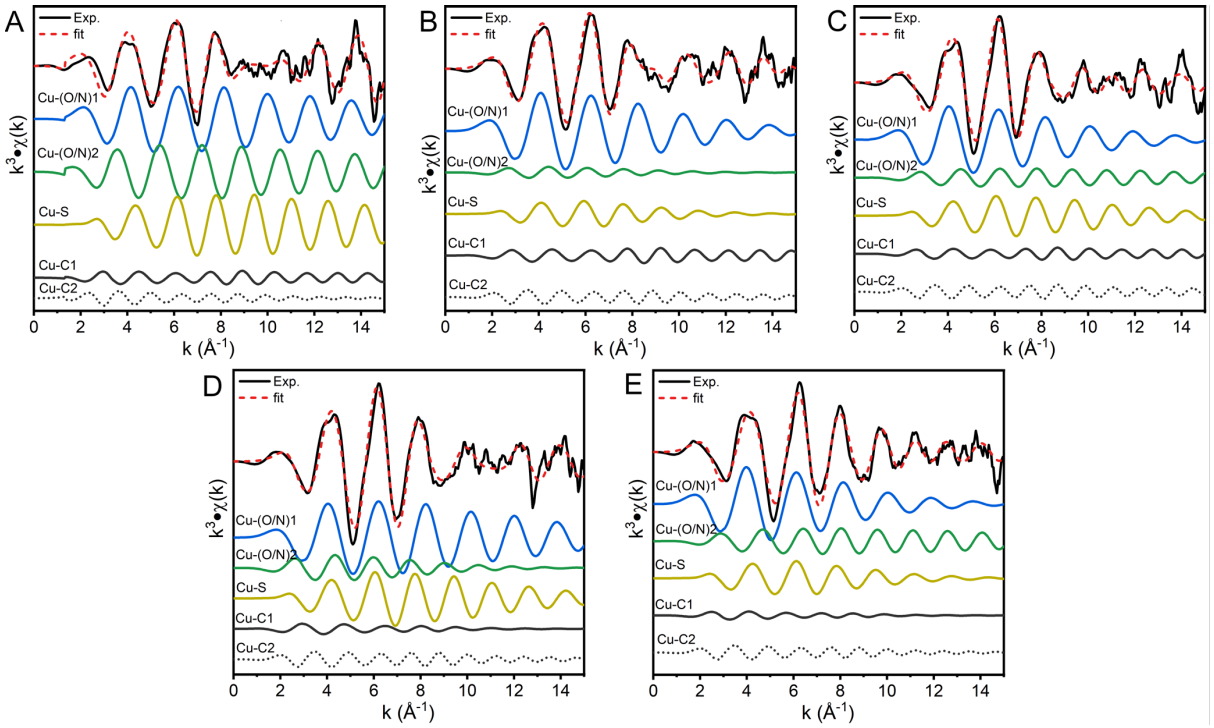

Figure S8. Comparison of Cu K-edge EXAFS spectra in k-space of HEAz variants A) HEAz, B) HESAz, C) HENAz, D) HENSAz, E) HEPAz. Fits corresponding to Table 5 (main text) are shown as dashed colored lines. Spectra are k^3-weighted.

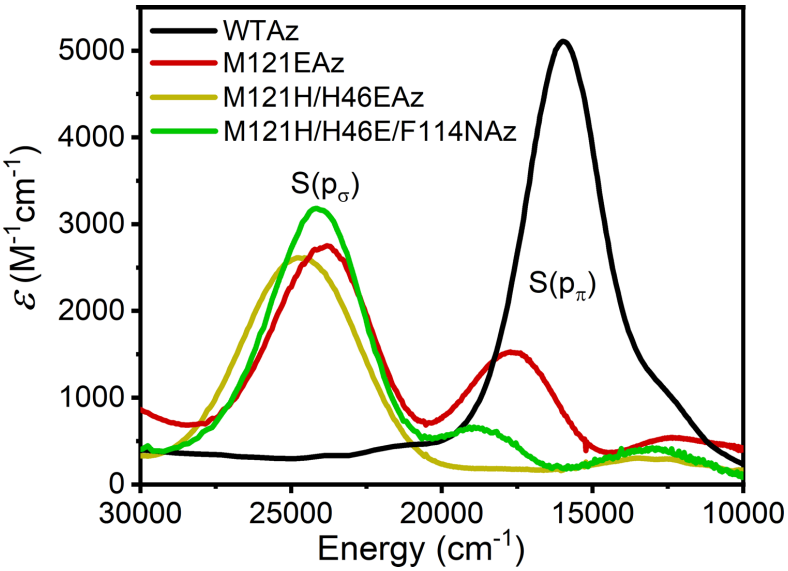

Figure S9. Comparison of the UV-Vis spectra of WTAz with Glu-substituted azurin (M121EAz, M121H/H46EAz), and with an additional F114N mutation. Extinction coefficients were determined by X-band EPR-based spin quantification. All variants are Cu^{II}-coordinated.

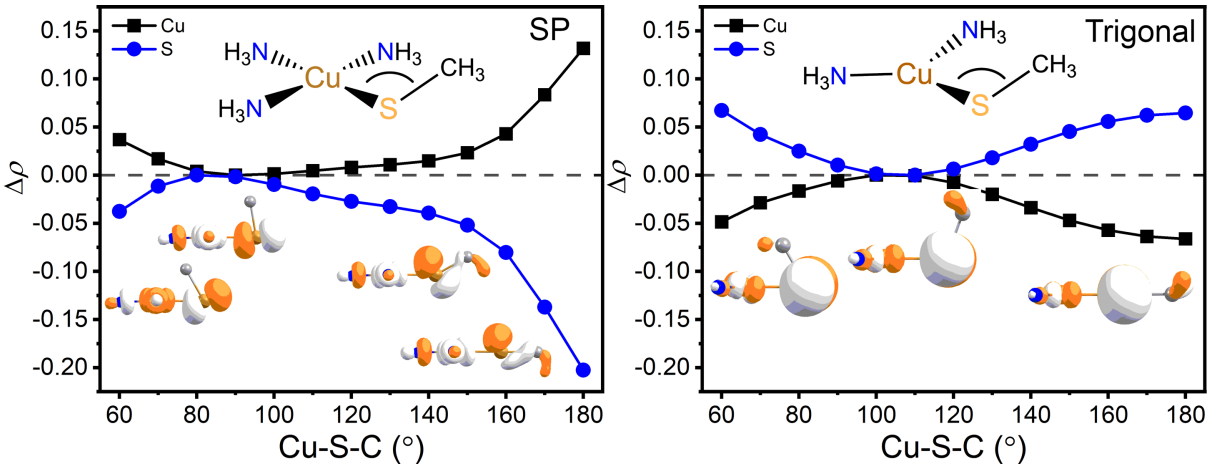

Figure S10. Variation in spin density at Cu and S for rigid scans of the Cu-S-C angle of a simplified $Cu^{II}(SCH_3)(NH_3)_x$ model for square planar (SP, x = 3, left) and trigonal (x = 2, right) geometries. The y-axis is provided as the change in spin density relative to either the maximum or minimum value along the coordinate. Calculations were performed at the TPSSh/DLPNO-CCSD level together with a def2-TZVP basis set. Representative isosurfaces are plotted for the SOMO orbital, and were rendered with an isovalue of 0.05.

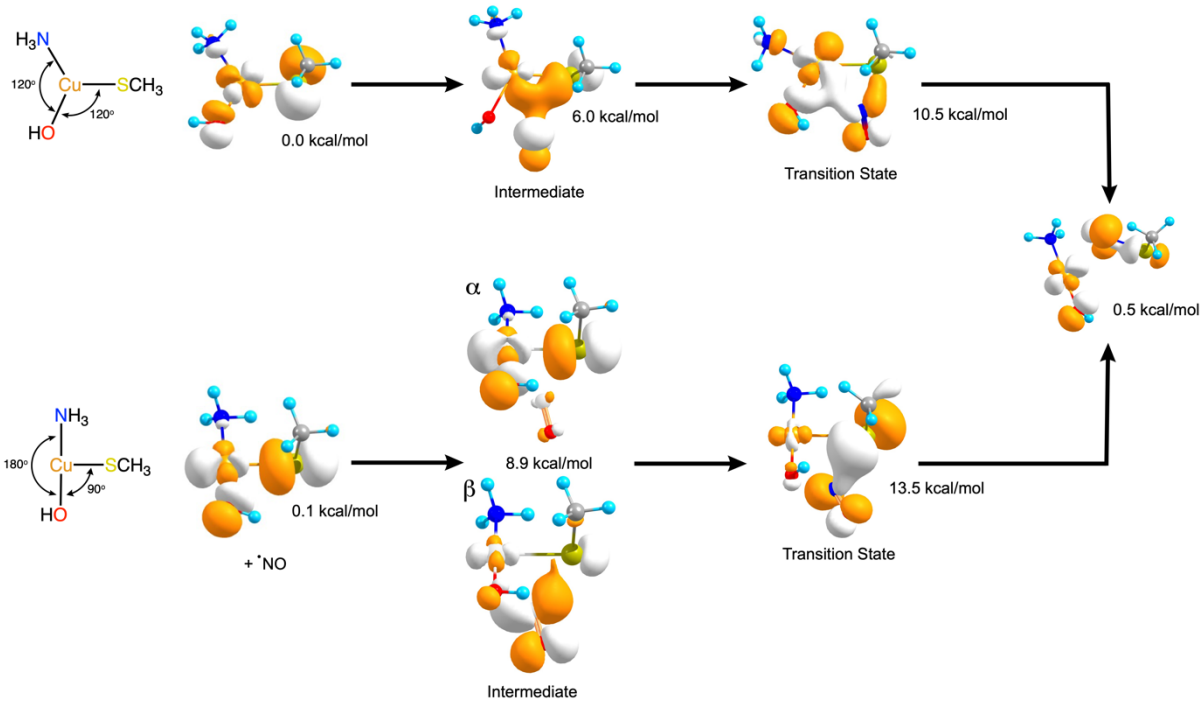

Figure S11. Reaction coordinate scans for attack of the Cu-S bond by •NO in planar T-shaped (with σ-type HOMO) and trigonal geometries (with π-type HOMO) of Cu^{II}. Geometries were maintained during the relaxed surface scan by restricting the S-Cu-N/O angles to 90° and 120°, respectively, and the C-S-Cu-N/O dihedral to 90/270° to maintain planarity. The singly occupied spin-up α-orbital is shown for the starting point of both geometries. Formation of a bridging NO intermediate is enthalpically facile, but incurs an entropic cost for NO binding. The intermediate species formed in the trigonal planar approach involves overlap of a single lobe of NO with the Cu-S π* interaction, where Cu is already formally reduced to Cu^{I}. The intermediate species formed in the square planar still formally contains Cu^{II}, which is strongly coupled (*J* of several thousand wavenumbers) to •NO. Transition states shown in both cases correspond with the barrier to Cu-N/Cu-S bond cleavage, where Cu^{I} is found in both geometries. Calculations were performed using the TPSSh hybrid functional together with a def2-TZVP basis set in an unrestricted Hartree-Fock formalism using a broken symmetry approach. All energies are presented as ΔG (kcal/mol). Isosurfaces were generated at 0.05.

Supplementary Tables

Table S1. Summary of energies and extinction coefficients of Gaussian deconvoluted UV/Vis spectra. Extinction coefficients (ε) were determined by X-band EPR quantification of [Cu^{II}].

	$S(p_\sigma)$		$S(p_\pi)$		d-d	
Variant (Az)	E (cm^{-1})	ε ($M^{-1}cm^{-1}$)	E (cm^{-1})	ε ($M^{-1}cm^{-1}$)	E (cm^{-1})	ε ($M^{-1}cm^{-1}$)
M121E	23900	2720	17700	1530	12400	380
M121H/H46E	24600	2770	18600	280	12900	370
M121H/H46E/47S	25800	2290	19500	220	13700	320
M121H/H46E/F114N	24100	3370	18800	680	13100	420
M121H/H46E/F114N/N47S	24900	1730	19100	340	13200	230
M121H/H46E/F114P	25600	2380	19500	270	13400	240

Table S2. Summary of band deconvolution analysis of Cu K-edge XAS spectra. All energies and half-width half-maximum (HWHM) values are provided in units of eV.

			Band				
			Shakedown			**Main**	
Variant	**Parameter**	**Pre-edge**	**1**	**2**	**3**	**1**	**2**
HEAz	Energy	8977.46	8982.33	8984.12	8986.15	8988.11	8991.06
	Amplitude	0.035	0.035	0.116	0.182	0.054	0.364
	HWHM	1.07	1.49	1.24	1.44	1.12	2.59
HESAz	Energy	8977.54	8982.33	8984.03	8986.07	8988.12	8991.06
	Amplitude	0.032	0.132	0.146	0.190	0.054	0.379
	HWHM	1.07	1.49	1.24	1.44	1.12	2.51
HENAz	Energy	8977.43	8982.33	8983.65	8985.63	8987.7	8991.00
	Amplitude	0.039	0.018	0.123	0.17	0.1384	0.352
	HWHM	0.94	1.49	1.08	1.15	1.19	2.69
HENSAz	Energy	8977.51	8982.23	8984.09	8985.97	8988.12	8991.31
	Amplitude	0.033	0.126	0.082	0.200	0.125	0.320
	HWHM	1.132	1.49	0.98	1.44	1.28	2.51
HEPAz	Energy	8977.58	8982.33	8984.12	8986.15	8988.12	8990.91
	Amplitude	0.029	0.077	0.100	0.173	0.059	0.325
	HWHM	0.91	1.49	1.24	1.44	1.12	2.74

Table S3. Comparison of EXAFS fits for degeneracies of 3/1 vs. 2/2 for scattering paths Cu-(O/N)1 and Cu-(O/N)2.

Variant	Scattering Path	*N*	R (Å)	σ^2 (10^{-3} Å^2)	E_0 (eV)	Red. χ^2	R-factor
HEAz	Cu-(O/N)1	3	2.00 ± 0.03	6.2 ± 1.1			
(3/1)	Cu-(O/N)2	1	2.25 ± 0.04	1.5 ± 0.2			
	Cu-S	1	2.29 ± 0.02	2.3 ± 1.5	8993 ± 5	124	0.017
	Cu-C1	1	2.52 ± 0.06	1.5 ± 0.2			
	Cu-C2	2	2.98 ± 0.03	3.7 ± 3.0			
HEAz	Cu-(O/N)1	2	2.00 ± 0.02	2.1 ± 0.7			
(2/2)	Cu-(O/N)2	2	2.20 ± 0.05	1.5 ± 0.5			
	Cu-S	1	2.27 ± 0.01	2.3 ± 1.0	8994 ± 3	68	0.013
	Cu-C1	1	2.59 ± 0.03	1.5 ± 0.3			
	Cu-C2	2	3.00 ± 0.03	5.9 ± 3.0			

HESAz	Cu-(O/N)1	3	1.97 ± 0.01	6.0 ± 0.8			
(3/1)	Cu-(O/N)2	1	2.49 ± 0.07	10.0 ± 3.0			
	Cu-S	1	2.30 ± 0.01	9.0 ± 2.0	8991 ± 2	103	0.011
	Cu-C1	1	2.51 ± 0.02	1.5 ± 0.1			
	Cu-C2	2	2.95 ± 0.03	4.1 ± 0.6			
HESAz	Cu-(O/N)1	2	1.96 ± 0.01	3.8 ± 1.0			
(2/2)	Cu-(O/N)2	2	2.53 ± 0.04	10.0 ± 3.0			
	Cu-S	1	2.24 ± 0.05	10.0 ± 1.0	8988 ± 3	224	0.019
	Cu-C1	1	2.50 ± 0.03	1.5 ± 0.2			
	Cu-C2	2	2.92 ± 0.03	5.0 ± 3.8			
HENAz	Cu-(O/N)1	3	1.99 ± 0.01	6.7 ± 0.8			
(3/1)	Cu-(O/N)2	1	2.44 ± 0.01	1.8 ± 1.2			
	Cu-S	1	2.26 ± 0.01	4.7 ± 1.0	8992 ± 1	100	0.009
	Cu-C1	1	2.64 ± 0.03	1.5 ± 0.3			
	Cu-C2	2	2.99 ± 0.02	3.0 ± 0.2			
HENAz	Cu-(O/N)1	2	1.96 ± 0.02	4.4 ± 3.0			
(2/2)	Cu-(O/N)2	2	2.44 ± 0.05	3.3 ± 1.2			
	Cu-S	1	2.23 ± 0.02	4.0 ± 0.4	8987 ± 6	133	0.014
	Cu-C1	1	2.64 ± 0.06	1.5 ± 1.5			
	Cu-C2	2	2.97 ± 0.04	2.7 ± 1.4			
HENSAz	Cu-(O/N)1	3	1.98 ± 0.01	3.1 ± 0.6			
(3/1)	Cu-(O/N)2	1	2.55 ± 0.06	10.0 ± 1.0			
	Cu-S	1	2.28 ± 0.01	3.8 ± 1.0	8993 ± 1	99	0.008
	Cu-C1	1	2.46 ± 0.07	10.0 ± 2.0			
	Cu-C2	2	2.97 ± 0.02	3.0 ± 1.0			
HENSAz	Cu-(O/N)1	2	1.97 ± 0.02	3.0 ± 0.6			
(2/2)	Cu-(O/N)2	2	2.51 ± 0.06	10.0 ± 1.0			
	Cu-S	1	2.26 ± 0.02	4.3 ± 2.0	8990 ± 4	163	0.014
	Cu-C1	1	2.46 ± 0.12	10.0 ± 2.0			
	Cu-C2	2	2.95 ± 0.03	5.1 ± 3.0			
HEPAz	Cu-(O/N)1	3	1.99 ± 0.01	8.7 ± 0.8			
(3/1)	Cu-(O/N)2	1	2.35 ± 0.04	4.3 ± 1.0			
	Cu-S	1	2.24 ± 0.01	5.0 ± 2.0	8990 ± 2	111	0.009
	Cu-C1	1	2.68 ± 0.01	10.0 ± 2.0			
	Cu-C2	2	2.96 ± 0.03	6.7 ± 1.0			
HEPAz	Cu-(O/N)1	2	1.96 ± 0.03	5.8 ± 2.4			
(2/2)	Cu-(O/N)2	2	2.38 ± 0.08	10.0 ± 1.0			
	Cu-S	1	2.23 ± 0.03	4.0 ± 2.0	8987 ± 4	172	0.015
	Cu-C1	1	2.67 ± 0.08	2.6 ± 0.5			
	Cu-C2	2	2.90 ± 0.05	7.7 ± 0.9			

Table S4. Summary of QM/MM calculated vibrational modes of the HEAz variants.

		Elemental Composition Factors					
Variant	Energy (cm^{-1})	C	O	N	H	S	Cu
HEAz	291	0.22	0.39	0.16	0.13	0.05	0.04
	306	0.31	0.13	0.23	0.07	0.07	0.19
	308	0.15	0.21	0.09	0.07	0.34	0.13
HESAz	292	0.26	0.31	0.23	0.09	0.04	0.07
	302	0.16	0.18	0.10	0.07	0.36	0.13
	320	0.36	0.24	0.11	0.18	0.08	0.03
HENAz	288	0.17	0.32	0.14	0.16	0.12	0.08
	306	0.24	0.34	0.13	0.08	0.06	0.14
	309	0.18	0.28	0.07	0.12	0.25	0.11
HENSAz	290	0.17	0.24	0.13	0.08	0.21	0.17
	309	0.18	0.41	0.28	0.11	0.02	0.01
	310	0.14	0.34	0.21	0.10	0.15	0.05
HEPAz	303	0.24	0.37	0.17	0.09	0.07	0.06
	325	0.24	0.23	0.25	0.10	0.13	0.05
	328	0.16	0.46	0.10	0.08	0.15	0.05

References

1. Rehr, J. J.; Kas, J. J.; Prange, M. P.; Sorini, A. P.; Takimoto, Y.; Vila, F., Ab initio theory and calculations of X-ray spectra. *Comp. Rend. Phys.* **2009,** *10*, 548-559.
2. Rehr, J. J.; Albers, R. C., Theoretical approaches to x-ray absorption fine structure. *Rev. Mod. Phys.* **2000,** *72*, 621-654.
3. Ankudinov, A. L.; Ravel, B.; Rehr, J. J.; Conradson, S. D., Real-space multiple-scattering calculation and interpretation of x-ray-absorption near-edge structure. *Phys. Rev. B* **1998,** *58*, 7565-7576.
4. Newville, M., Larch: An Analysis Package for XAFS and Related Spectroscopies. *J. Phys.* **2013,** *430*.
5. Tian, S.; Liu, J.; Cowley, R. E.; Hosseinzadeh, P.; Marshall, N. M.; Yu, Y.; Robinson, H.; Nilges, M. J.; Blackburn, N. J.; Solomon, E. I.; Lu, Y., Reversible S-nitrosylation in an engineered azurin. *Nat. Chem.* **2016,** *8*, 670-7.
6. Bjornsson, R. *ASH - a multiscale modelling program*, 9.0; 2022.
7. Neese, F., The ORCA program system. *WIREs Comp. Mol. Sci.* **2012,** *2*, 73-78.
8. Neese, F., Software update: the ORCA program system, version 4.0. *WIREs Comp. Mol. Sci.* **2018,** *8*, e1327.
9. Best, R. B.; Zhu, X.; Shim, J.; Lopes, P. E. M.; Mittal, J.; Feig, M.; MacKerell, A. D., Jr., Optimization of the Additive CHARMM All-Atom Protein Force Field Targeting Improved Sampling of the Backbone ϕ, ψ and Side-Chain χ1 and χ2 Dihedral Angles. *J. Chem. Theory Comp.* **2012,** *8*, 3257-3273.
10. Schulz, C. E.; van Gastel, M.; Pantazis, D. A.; Neese, F., Converged Structural and Spectroscopic Properties for Refined QM/MM Models of Azurin. *Inorg. Chem.* **2021,** *60*, 7399-7412.
11. Sherwood, P.; de Vries, A. H.; Guest, M. F.; Schreckenbach, G.; Catlow, C. R. A.; French, S. A.; Sokol, A. A.; Bromley, S. T.; Thiel, W.; Turner, A. J.; Billeter, S.; Terstegen, F.; Thiel, S.; Kendrick, J.; Rogers, S. C.; Casci, J.; Watson, M.; King, F.; Karlsen, E.; Sjøvoll, M.; Fahmi, A.; Schäfer, A.; Lennartz, C., QUASI: A general purpose implementation of the QM/MM approach and its application to problems in catalysis. *J. Mol. Struct.* **2003,** *632*, 1-28.

12. Tao, J.; Perdew, J. P.; Staroverov, V. N.; Scuseria, G. E., Climbing the Density Functional Ladder: Nonempirical Meta--Generalized Gradient Approximation Designed for Molecules and Solids. *Phys. Rev. Lett.* **2003,** *91*, 146401.
13. Staroverov, V. N.; Scuseria, G. E.; Tao, J.; Perdew, J. P., Comparative assessment of a new nonempirical density functional: Molecules and hydrogen-bonded complexes. *J. Chem. Phys.* **2003,** *119*, 12129-12137.
14. Grimme, S.; Antony, J.; Ehrlich, S.; Krieg, H., A consistent and accurate ab initio parametrization of density functional dispersion correction (DFT-D) for the 94 elements H-Pu. *J. Chem. Phys.* **2010,** *132*, 154104.
15. Grimme, S.; Ehrlich, S.; Goerigk, L., Effect of the damping function in dispersion corrected density functional theory. *J. Comp. Chem.* **2011,** *32*, 1456-1465.
16. Douglas, M.; Kroll, N. M., Quantum electrodynamical corrections to the fine structure of helium. *Ann. Phys.* **1974,** *82*, 89-155.
17. Hess, B. A., Applicability of the no-pair equation with free-particle projection operators to atomic and molecular structure calculations. *Phy.s Rev. A Gen. Phys.* **1985,** *32*, 756-763.
18. Hess, B. A., Relativistic electronic-structure calculations employing a two-component no-pair formalism with external-field projection operators. *Phys. Rev. A Gen. Phys.* **1986,** *33*, 3742-3748.
19. Wolf, A.; Reiher, M.; Hess, B. A., The generalized Douglas–Kroll transformation. *J. Chem. Phys.* **2002,** *117*, 9215-9226.
20. Weigend, F.; Ahlrichs, R., Balanced basis sets of split valence, triple zeta valence and quadruple zeta valence quality for H to Rn: Design and assessment of accuracy. *Phys. Chem. Chem. Phys.* **2005,** *7*, 3297-305.
21. Pantazis, D. A.; Chen, X. Y.; Landis, C. R.; Neese, F., All-Electron Scalar Relativistic Basis Sets for Third-Row Transition Metal Atoms. *J. Chem. Theory Comput.* **2008,** *4*, 908-19.
22. Weigend, F., Accurate Coulomb-fitting basis sets for H to Rn. *Phys. Chem. Chem. Phys.* **2006,** *8*, 1057-65.
23. Neese, F.; Wennmohs, F.; Hansen, A.; Becker, U., Efficient, approximate and parallel Hartree–Fock and hybrid DFT calculations. A 'chain-of-spheres' algorithm for the Hartree–Fock exchange. *Chem. Phys.* **2009,** *356*, 98-109.
24. Saitow, M.; Becker, U.; Riplinger, C.; Valeev, E. F.; Neese, F., A new near-linear scaling, efficient and accurate, open-shell domain-based local pair natural orbital coupled cluster singles and doubles theory. *J. Chem. Phys.* **2017,** *146*, 164105.
25. Sparta, M.; Retegan, M.; Pinski, P.; Riplinger, C.; Becker, U.; Neese, F., Multilevel Approaches within the Local Pair Natural Orbital Framework. *J. Chem. Theory Comput.* **2017,** *13*, 3198-3207.
26. Nar, H.; Messerschmidt, A.; Huber, R.; van de Kamp, M.; Canters, G. W., Crystal structure analysis of oxidized Pseudomonas aeruginosa azurin at pH 5.5 and pH 9.0. A pH-induced conformational transition involves a peptide bond flip. *J. Mol. Biol.* **1991,** *221*, 765-72.
27. Cheung, K. C.; Strange, R. W.; Hasnain, S. S., 3D EXAFS refinement of the Cu site of azurin sheds light on the nature of structural change at the metal centre in an oxidation-reduction process: an integrated approach combining EXAFS and crystallography. *Acta Crystallogr. D Biol. Crystallogr.* **2000,** *56*, 697-704.
28. Shadle, S. E.; Penner-Hahn, J. E.; Schugar, H. J.; Hedman, B.; Hodgson, K. O.; Solomon, E. I., X-ray absorption spectroscopic studies of the blue copper site: metal and ligand K-edge studies to probe the origin of the EPR hyperfine splitting in plastocyanin. *J. Am. Chem. Soc.* **1993,** *115*, 767-776.
29. DeBeer, S.; Randall, D. W.; Nersissian, A. M.; Valentine, J. S.; Hedman, B.; Hodgson, K. O.; Solomon, E. I., X-ray Absorption Edge and EXAFS Studies of the Blue Copper Site in Stellacyanin: Effects of Axial Amide Coordination. *J. Phys. Chem. B* **2000,** *104*, 10814-10819.